RZ 3935 (# ZUR1808-057) 08/31/2018
Physical Sciences 7 pages

Research Report

Concurrent Zinc-Blende and Wurtzite Film Formation by Selection of Confined Growth Planes

P. Staudinger, S. Mauthe, K. Moselund, H. Schmid

IBM Research – Zurich
8803 Rüschlikon
Switzerland

This article has been published in *Nano Letters* **2018** *18* (12), 7856-7862
DOI: 10.1021/acs.nanolett.8b03632 as an open access article under an ACS AuthorChoice License, which permits copying and redistribution of the article or any adaptations for non-commercial purposes.

NANO LETTERS

Letter

Cite This: Nano Lett. 2018, 18, 7856−7862

pubs.acs.org/NanoLett

Concurrent Zinc-Blende and Wurtzite Film Formation by Selection of Confined Growth Planes

Philipp Staudinger, Svenja Mauthe, Kirsten E. Moselund, and Heinz Schmid*

IBM Research - Zürich, Säumerstrasse 4, 8803 Rüschlikon, Switzerland

ABSTRACT: Recent research on nanowires (NWs) demonstrated the ability of III−V semiconductors to adopt a different crystallographic phase when they are grown as nanostructures, giving rise to a novel class of materials with unique properties. Controlling the crystal structure however remains difficult and the geometrical constraints of NWs cause integration challenges for advanced devices. Here, we report for the first time on the phase-controlled growth of micron-sized planar InP films by selecting confined growth planes during template-assisted selective epitaxy. We demonstrate this by varying the orientation of predefined templates, which results in concurrent formation of zinc-blende (ZB) and wurtzite (WZ) material exhibiting phase purities of 100% and 97%, respectively. Optical characterization revealed a 70 meV higher band gap and a 2.5× lower lifetime for WZ InP in comparison to its natural ZB phase. Further, a model for the transition of the crystal structure is presented based on the observed growth facets and the bonding configuration of InP surfaces.

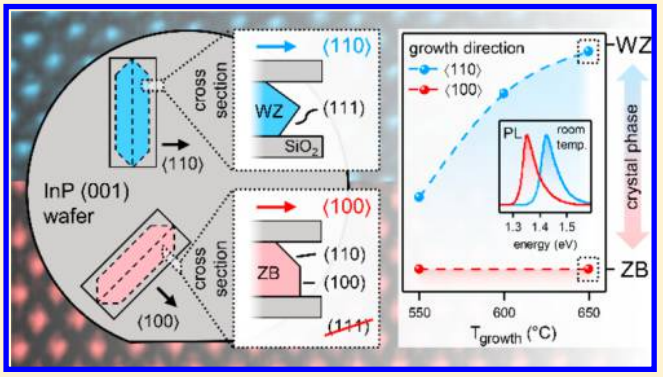

KEYWORDS: *Crystal structure, zinc-blende, wurtzite, indium phosphide, template-assisted selective epitaxy*

Group III−V semiconductor nanostructures are key components for high-speed electronic,[1] optoelectronic,[2] and photovoltaic[3] applications due to their favorable material properties and the flexibility to employ various kinds of heterostructures.[4] One of the main challenges is the formation of high-quality material, because nanostructures and in particular grown NWs typically suffer from high densities of planar defects (PDs) such as rotational twins and stacking faults. PDs lead to lower performance by reducing quantum efficiency, carrier lifetime, and mobility as well as introducing nonradiative recombination centers and scattering planes.[5−7] Moreover, the control of the crystal phase is of key importance because, for example, for InP it has been reported both theoretically[8,9] and experimentally[10,11] that the band structure varies significantly between the cubic ZB and the related hexagonal WZ structure resulting in a bandgap energy difference of about 70 meV and type-II superlattices if they are intermixed.[12,13] While it is obvious that uncontrolled polytypism limits the opportunities for applications, the possibility to selectively tune electronic and optical properties within the same material system by crystal phase engineering results in a unique degree of freedom for enhancing the functionality of emerging devices. Spirkoska et al. demonstrated the spatial carrier confinement in quantum-well structures formed by ZB/WZ heterostructures in GaAs,[14] whereas other materials such as GaP, AlP, and Ge even change the bandgap from indirect to direct when the crystal structure is converted from cubic to hexagonal.[8,15,16] These findings recently enabled efficient emission in the amber-green region of the visible spectrum from AlInP NWs[17] and may pave the way toward SiGe light sources with a bandgap close to the telecommunication wavelength.[18] So far, however, the crystal phase remains challenging to control and phase intermixing is a commonly observed problem for III−V integration.[19−21] In addition, the two most explored techniques, vapor−liquid−solid (VLS)[22] and selective area growth,[23] cannot surmount the size constraints of NWs with diameters below a few hundreds of nanometers causing fundamental challenges for device integration which is conventionally based on planar structures.

In this study, we report on micron-sized InP layers epitaxially deposited inside hollow SiO_2 cavities on top of an InP(001) substrate. We demonstrate that the crystal structure can be controlled by confining and guiding the growth along specific crystalline directions, namely ⟨100⟩ and ⟨110⟩ for ZB and WZ, respectively. Thus, we achieve simultaneous formation of planar films exhibiting both crystal phases at sizes up to 50 μm^2. Crystal structure and defects are characterized by scanning transmission electron microscopy (STEM) along with microphotoluminescence (μ-PL) measurements and are found to be pure and without defects for ZB and with a stacking-purity of about 97% for WZ crystals. This is the first report demonstrating the fabrication of micron-sized WZ InP layers, thus opening new pathways for exploring fundamental material properties as well as establishing novel

Received: September 7, 2018
Revised: October 29, 2018
Published: November 14, 2018

DOI: 10.1021/acs.nanolett.8b03632
Nano Lett. 2018, 18, 7856−7862

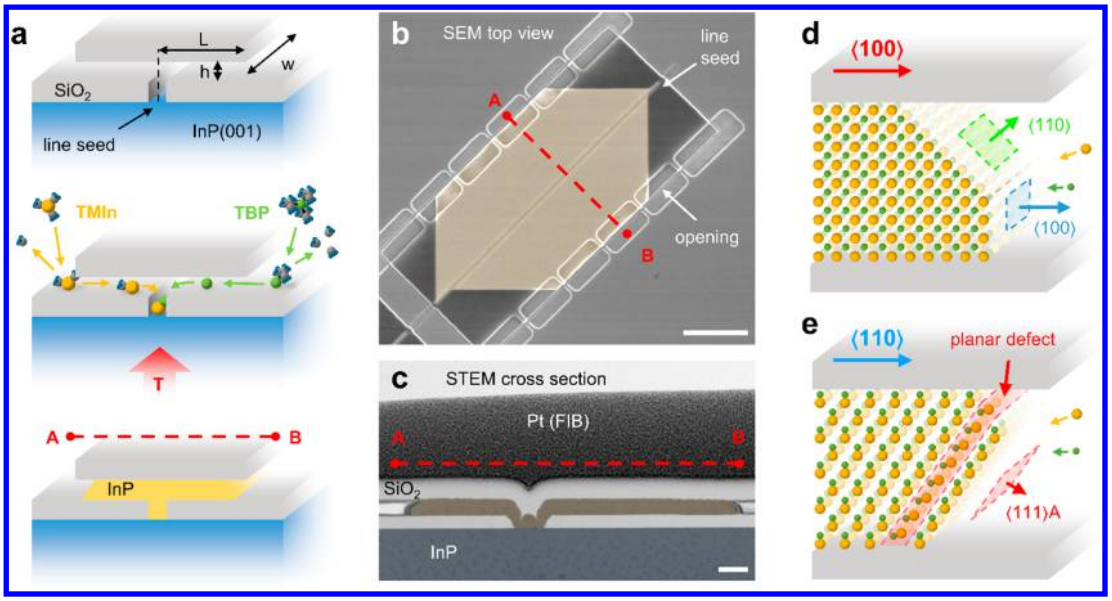

Figure 1. Experimental implementation of confined growth planes. (a) From top to bottom: empty SiO_2 cavity as processed on top of an InP(001) substrate, sketch of the selective epitaxy process, and template after MOCVD growth. (b) SEM top view image of an InP crystal after growth (colored in yellow). The crystal expands from the central line seed toward the openings. Scale bar: 1 μm. (c) Low-resolution BF-STEM image showing the cross section of a crystal (yellow) on top of the InP(001) substrate (blue). Scale bar: 100 nm. (d,e) Illustrations to show faceting along different growth orientations. {111} facets and therefore PDs can only be formed when the crystals are grown along ⟨110⟩.

devices. Although InP was used as a model system, to some extent these findings are expected to be valid also for other compound semiconductor materials.

To grow InP films on InP(001), we employ a method similar to template-assisted selective epitaxy (TASE)[24] but using much larger and elongated seed areas as reported in tunnel epitaxy,[25] confined lateral selective epitaxial growth,[26] or conformal vapor phase epitaxy.[27] In essence, we pattern line seeds on top of SiO_2 covered InP(001) substrates, which are aligned along various crystalline orientations and capped again with an SiO_2 layer (Figure 1a top). Selective epitaxy of InP is carried out in an MOCVD reactor using trimethylindium (TMIn) and tertiarybutylphosphine (TBP) at a V/III precursor ratio of 100 and variable temperatures (T_{growth}) until the templates (L = 1 μm) are filled (Figure 1a bottom). Growth rates are in the range of 0.5−1 μm/h depending on reactor conditions with excellent selectivity to the SiO_2 cavity. See Methods for more details on the process. An SEM top view micrograph of a typical crystal exhibiting a width w = 5 μm is depicted in Figure 1b. Clear faceting demonstrates the homoepitaxial and single-crystalline nature of the deposition process and was observed irrespective of template width up to 50 μm (the widest investigated in this study). A cross sectional low-resolution bright field (BF)-STEM image of another crystal is shown in Figure 1c.

To demonstrate the effect of confined growth planes we compare films grown from two different template orientations. In the first case the line seed is oriented along ⟨100⟩ and the crystals thus grow along another ⟨100⟩ direction perpendicular to it (Figure 1d). Given that there is a single growth front in parallel to the seed line, which is typically observed in our experiments (compare Figure 1b), the local growth direction must lie within the plane perpendicular to this seed line. Low order facets in this direction include {100} and {110}, but notably no {111} facets along which PDs could be formed. Thus, we expect pure ZB phase for crystals grown along this direction.[21] InP grown along a ⟨110⟩ orientation in contrast allows for different faceting, since both ⟨111⟩A and ⟨111⟩B directions are available locally and hence we expect to obtain PDs as indicated in Figure 1e. In the second case, controlling the stacking sequence would yield the possibility to transform the crystal phase from ZB (ABC stacking) to other polytypes such as the WZ structure (ABAB stacking).

First, we characterize crystals grown along the ⟨100⟩ direction using STEM. Figure 2a depicts a representative high-angle annular dark field (HAADF) image of a film grown at standard conditions for InP growth (T_{growth} = 550 °C, V/III = 100). Note that the zone axis is [−110] and thus not

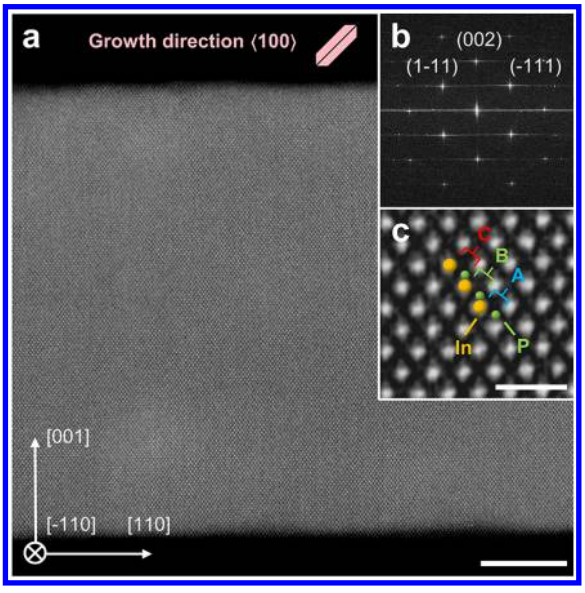

Figure 2. STEM investigation of an InP crystal grown along ⟨100⟩. (a) Cross-sectional overview of the film with height h = 50 nm. Scale bar: 10 nm. (b) Corresponding FFT pattern showing ZB symmetry. (c) HR-image demonstrating the ABC type stacking. Scale bar: 1 nm.

DOI: 10.1021/acs.nanolett.8b03632
Nano Lett. 2018, 18, 7856−7862

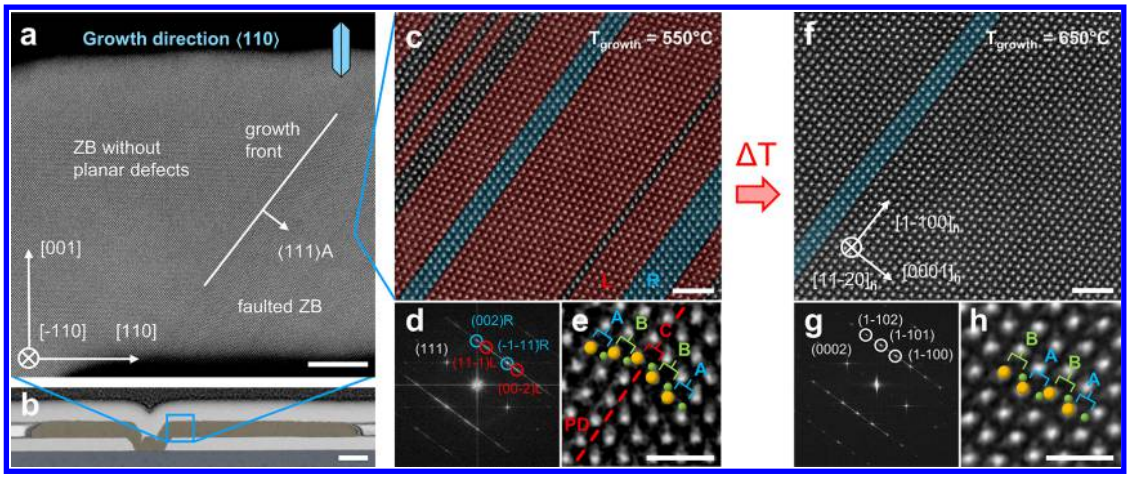

Figure 3. STEM investigation of InP films grown along ⟨110⟩. (a,b) Cross-sectional overview of the crystal with height h = 50 nm close to the seed area. Scale bars: 10 and 100 nm. (c,f) HR-STEM images of InP crystals grown at 550 and 650 °C, respectively. Colored areas represent ZB segments with the two possible stacking orientations (ABC, CBA). Scale bars: 2 nm. (d,f) Corresponding FFT patterns showing faulted ZB and WZ symmetry, respectively. (e,h) Detailed micrographs of the crystal stacking. Scale bars: 1 nm.

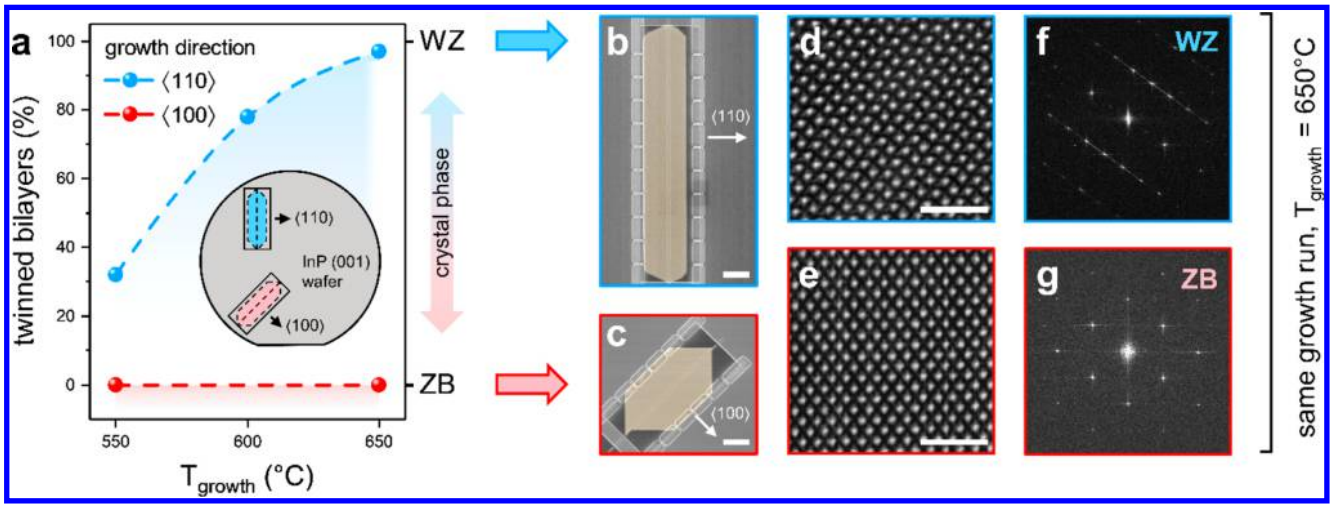

Figure 4. Simultaneous growth of ZB and WZ InP layers. (a) Number of twinned bilayers as a function of growth temperature for InP films grown along ⟨110⟩ and ⟨100⟩. Simultaneous formation is achieved at 650 °C. (b,c) Colored top-view SEM images of typical crystals. Scale bars: 1 μm. (d,e) HR-STEM images of InP crystals grown along ⟨110⟩ and ⟨100⟩, respectively. Scale bars: 2 nm. (f,g) Corresponding FFT patterns showing WZ and ZB symmetry, respectively.

perpendicular to the growing direction but rotated by 45°. The entire cross-section of the h = 50 nm high film is shown in this image. We have not found any defects along the entire crystal and thus pure ZB phase is obtained, which is attributed to the specific growth geometry and the related absence of {111} facets. Figure 2b,c depict the corresponding fast Fourier transform (FFT) pattern as well as a high-resolution (HR)-STEM image showing the ABC type ZB stacking.

Similarly, an InP film grown with identical conditions but along the ⟨110⟩ direction is shown in Figure 3a–e. First, we investigate the area close to the beginning of the growth as seen from the [−110] zone axis indicated in the BF-STEM micrograph in Figure 3b. We typically observe pure ZB InP without PDs for the first few tens of nanometers (Figure 3a) but as soon as the first PD occurs we immediately obtain a high defect density (~1 PD/nm), as it is depicted in more detail in Figure 3c. We therefore conclude that the crystal as it is expanding from the horizontal substrate follows growth directions deviating from ⟨111⟩ in the beginning, however as soon as the (111)A facet is present it remains stable and PDs can be formed easily due to its high susceptibility to twinning. The presence of these PDs also manifests itself in the corresponding FFT pattern presented in Figure 3d. A single rotational twin and the related inversion of the stacking sequence is depicted in Figure 3e in more detail. In a second experiment, the growth temperature is increased by 100 °C to T_{growth} = 650 °C by ramping up from 600 °C within the first 5 min to prevent desorption of the otherwise unstable InP (001) surface under the growth conditions accessible in our MOCVD reactor. As shown in Figures 3f the number of ZB segments is reduced strongly. Although only a small area is shown in this image, we observe similar crystal quality and defect density throughout the entire template, apart from the area close to the seed. The characteristic FFT pattern and ABAB stacking sequence along the $[0001]_h$ direction are clearly visible in Figure 3g,h demonstrating the formation of nearly pure WZ material. At the beginning of the growth, we obtain pure ZB material again, followed by a short polytypic region (~20 nm), which we believe originates from the temperature ramping procedure.

DOI: 10.1021/acs.nanolett.8b03632
Nano Lett. 2018, 18, 7856−7862

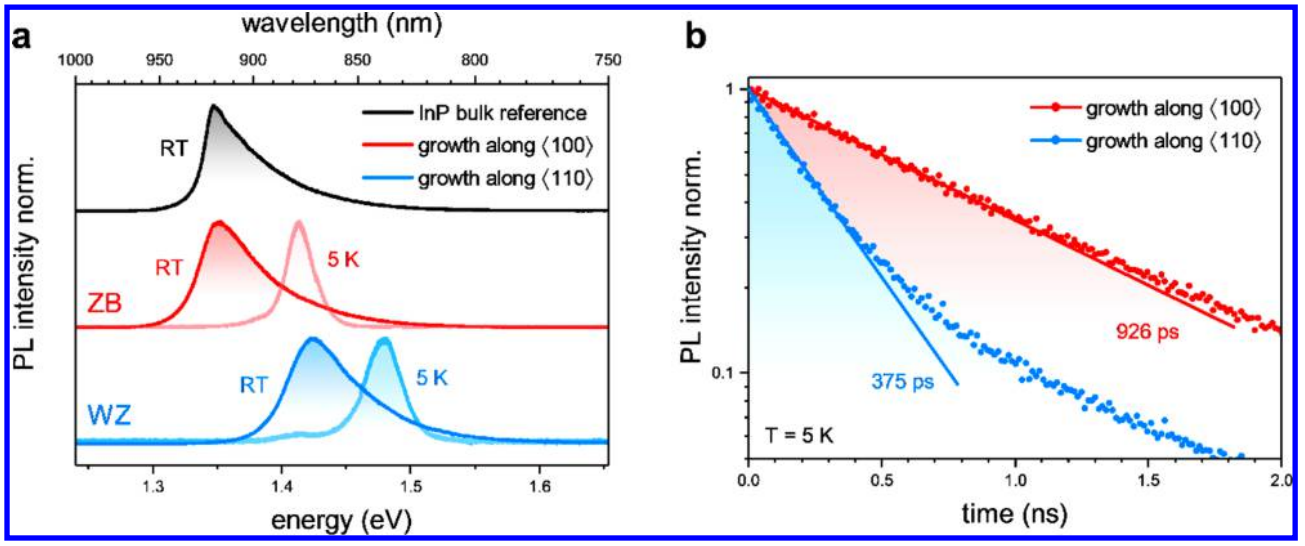

Figure 5. PL measurements of ZB and WZ InP films. (a) Normalized emission spectra of typical crystals along with bulk InP(001) at RT as well as 5 K. (b) Normalized TRPL measurements at 5 K demonstrate lifetime differences of ZB and WZ InP crystals exhibiting the exact same morphology.

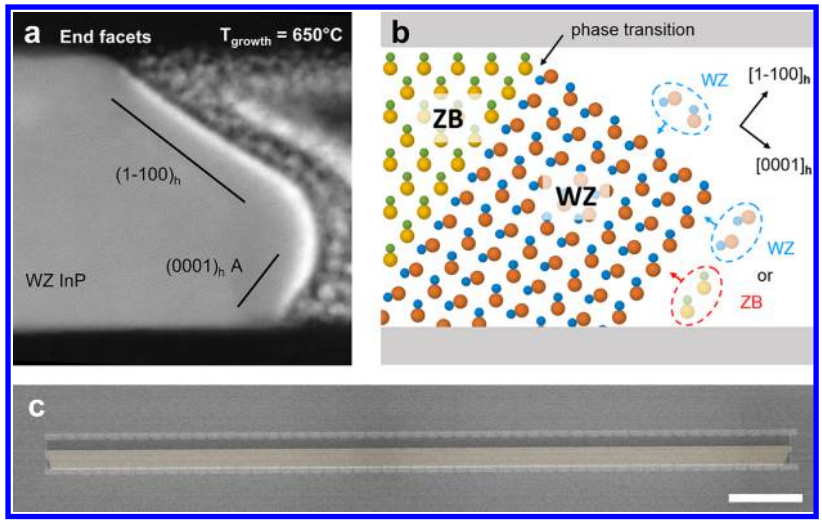

Figure 6. (a) End facets of a typical InP film grown in ⟨110⟩ direction and exhibiting WZ phase. (b) Atomistic model for structural transition in InP crystals. The variable stacking axis along the $[0001]_h$ A direction allows for an initial phase transition, which needs to be maintained during growth by forming nuclei at the edge toward the $(1\text{-}100)_h$ facet. In $[1\text{-}100]_h$ direction the stacking is strongly fixed and the WZ structure is transferred irrespective of growth conditions. (c) WZ InP film exhibiting a width w = 50 μm and a length L = 1 μm demonstrating the scalability of this approach. Scale bar: 5 μm.

We use statistical analysis proposed by Joyce et al.[28] to quantify the crystalline purity of our InP films. Every deviation from the perfect ZB stacking order (ABC) is accounted for as a single twinned bilayer (e.g. AB$\underline{A}$). As the proportion of twinned bilayers in ZB InP is increased from 0 to 100%, the crystal phase is thus transferred to pure WZ. In Figure 4a, we employ this analysis for different growth temperatures and directions by counting PDs in HR-STEM images. We observe that the number of twinned bilayers increases with temperature from 32% to 97% for films grown along ⟨110⟩ to nearly pure WZ at 650 °C. InP grown in ⟨100⟩-direction on the other hand remains free of PDs and is pure ZB in any case. Hence, we achieve simultaneous formation of both phases during the same growth run as demonstrated in Figure 4b–g. Increasing the temperature further is expected to result in even higher phase purity, however the TBP pressure in our MOCVD reactor was not sufficient to stabilize the InP surface under such conditions.

To further confirm the crystal phase transition and purity, we perform μ-PL on individual crystals after removal from the underlying InP substrate to exclude measurement interferences (see Methods for more details). Figure 5a depicts representative μ-PL emission spectra of InP crystals grown along ⟨100⟩ and ⟨110⟩ respectively, as well as of bulk InP as a reference. The PL measurements reveal a blueshift of about 70 meV for crystals grown along ⟨110⟩ with respect to bulk InP and crystals grown along the ⟨100⟩ direction. This shift, which is clearly observed for room temperature (RT) and low T measurements, is thus attributed to the phase change of the material. For WZ InP, we extract band gap energies corresponding to 1.41 and 1.47 eV for 293 and 5 K, respectively, which is in excellent agreement with previous reports on WZ InP NWs.[12,29] Additionally, at low T we obtain

DOI: 10.1021/acs.nanolett.8b03632
Nano Lett. 2018, 18, 7856−7862

a much smaller emission peak exactly at the position of bulk InP. This is believed to be due to the area close to the seed line which is ZB irrespective of template orientation. The fwhm of the spontaneous emission peaks for crystals grown along ⟨100⟩ and ⟨110⟩ is comparable to the one measured for bulk InP indicating high material quality and phase purity. Further, we use time-resolved PL (TRPL) to assess the overall effective carrier lifetime in our InP films. In Figure 5b we compare TRPL-measurements performed at 5 K from two crystals obtained during the same growth run and having the same defined morphology, the only difference being the growth direction and thus crystal phase. We obtain a 2.5-fold longer lifetime for ZB InP. According to the equivalent crystal morphology and assuming that there is no fundamental difference between the quality of the WZ and ZB InP surfaces, we thus conclude that the shorter exciton recombination lifetimes are an inherent property of the crystal phase and reflect the increased oscillator strength of the optical transition at the Γ-point.[30,31] These findings suggest the enhanced light emission from WZ InP as compared to its natural ZB crystal structure, which could result in more efficient light sources.

Next, we describe a model to explain the structural transition observed in crystals grown along the ⟨110⟩ direction. It is crucial to understand which type of facets are formed during the deposition process as they have a substantial influence on the growth dynamics. For example, PDs, which are essential to facilitate a phase transition, are exclusively formed along either the ZB ⟨111⟩A or ⟨111⟩B direction. In Figure 6a, we show the end facets of a typical WZ InP film, which consist out of a relatively small $(0001)_h$ A facet at the bottom and a larger $(1\text{-}100)_h$ facet perpendicular to it. As sketched in Figure 6b, the stacking sequence can easily be changed along the $\langle 0001\rangle_h$ direction which corresponds to the ⟨111⟩ direction in ZB. Hence, a transition from ZB to WZ is possible without introducing miscoordinated atoms.[32]

The question remains, why under certain conditions WZ stacking is preferred over ZB, which is known to be more stable in bulk form. Earlier experiments on vapor−liquid−solid (VLS) grown NWs suggest that once a nucleus of critical size is formed it spreads out laterally over the entire surface resulting in a layer-by-layer deposition mechanism.[33,34] The orientation of the initial nuclei for every layer therefore determines the stacking sequence and thus the crystal phase of the resulting material. It is further known from VLS growth that if such a nucleus is formed at the edge to the $(1\text{-}100)_h$ facet, WZ is preferred to minimize the overall surface energy, otherwise ZB stacking is energetically more favorable under typical growth conditions.[35,36] Hence, it is important to control the position of the nuclei on the $(0001)_h$ A surface to achieve control over the crystal phase.

Keeping this information in mind, we can have a closer look at the InP (111)A/$(0001)_h$ A surface. It is reported both theoretically[37] and experimentally[38] that its surface reconstruction is either In-rich (2 × 2) or P-rich (3 × 3)$R30°$ depending on growth temperature and precursor partial pressures. In the former case, which is at high T_{growth},[37] to proceed growth on the In-terminated surface, P atoms need to be adsorbed first. However, this bonding configuration is thought to be weak since it has only a single bond toward the surface, and the P atoms are desorbed easily.[4] We thus speculate that under such conditions the formation of nuclei exceeding the critical size becomes unlikely at the surface. Instead new layers start to form at the edge toward the $(1\text{-}100)_h$ facet where a high amount of dangling bonds is available and WZ phase is preferred in analogy to the existing models for the much more explored VLS technique.[35] This model can explain how the WZ phase becomes more dominant at higher T_{growth}, because the direct nucleation at the surface is suppressed and new nuclei are forced to be formed at the edge line. This is also in agreement with the fact that we observe a decrease of the growth rate when T_{growth} is increased from 550 to 650 °C.

Our model suggests that a low ratio between the $(0001)_h$A surface and its accompanying edge to the neighboring $(1\text{-}100)_h$ facet is required to prevent ZB nucleation on the $(0001)_h$A surface. Because in NW growth this ratio scales with diameter, stable WZ formation has not been observed in NWs exceeding a few hundred nanometers, nor in any planar epitaxy. For the same reason, increasing the height (h) of InP films grown by TASE is expected to result in polytypic material at a certain point. However, this ratio is constant irrespective of another parameter in our constrained geometry: the template width (w). We do not believe that there is any restriction to this value, which would enable the growth of arbitrarily wide crystals in a planar way. This was demonstrated by growing WZ films exhibiting an area of 50 μm^2, as shown in Figure 6c. Using such planar films as virtual substrates by subsequently transferring the crystal phase in vertical direction holds great promise for integrating more complex WZ thin-film heterostructures, perfectly suited for electro-optical devices.

In conclusion, by carefully selecting confined growth planes using TASE, we achieved the concurrent growth of pure ZB and nearly pure WZ InP films. Thus, we demonstrated a new pathway for facilitating complete phase transitions in a III−V material system. STEM, FFT, and PL analysis revealed the phase purity and optical quality of the obtained crystals and demonstrated a blueshift for the WZ phase in agreement with earlier literature reports on WZ InP NWs. By TRPL measurements, we obtained lower exciton lifetimes in the WZ phase which is a strong indicator for the increased oscillator strength of the optical transition and the resulting enhanced light emission of the material. We further proposed a model to describe our findings and demonstrated the scalability of our approach by growing WZ InP at sizes up to 50 μm^2. Remarkably, the growth of WZ InP has only been demonstrated in NW structures with the first WZ film formation shown in this work. Our study provides a new route for facilitating phase transitions in large area III−V material growth, which could bring us one step closer to the integration of a new class of optical devices with outstanding properties.

METHODS

Template Fabrication. Line seeds with nominal widths of 50 nm were patterned along the ⟨100⟩ and ⟨110⟩ direction on a standard InP(001) wafer covered with 50 nm plasma-enhanced chemical vapor deposited (PECVD) SiO_2 by e-beam lithography (EBL), reactive ion etching (RIE), and buffered hydrofluoric acid (BHF). Seeds were protected with 4 nm atomic-layer deposited (ALD) Al_2O_3 after which 50 or 100 nm amorphous Si (α-Si) was sputtered for structural and optical characterization, respectively. Sacrificial structures were patterned perpendicular to the seed lines with varying widths and lengths using EBL, inductively coupled plasma (ICP)-RIE, and a short diluted HF (DHF) dip to remove the Al_2O_3 after which the actual 50 nm thick SiO_2 templates are deposited

DOI: 10.1021/acs.nanolett.8b03632
Nano Lett. 2018, 18, 7856−7862

using ALD. The SiO_2 is opened at the position furthest away from the seed line using EBL, RIE, and DHF, and the α-Si within is etched using XeF_2 chemistry. Finally, the protective Al_2O_3 at the seed line is removed by DHF directly before the growth.

InP Growth. InP film growth was performed by MOCVD using TBP and TMIn at a total pressure of 60 Torr. Partial pressures for TBP and TMIn were kept at 8.2 Pa and 82 mPa, respectively, to achieve a nominal V/III ratio of 100. Upon loading, the reactor was heated in a TBP atmosphere, and deposition was initiated subsequently by introducing TMIn. Growth temperature was held constant for growth at 550 and 600 °C and ramped up from 600 °C within the first 5 min for growth at 650 °C to prevent desorption of the thermally unstable InP(001) substrate surface at the seed line. Growth times were varied between 40 and 60 min. After growth, substrates were cooled under a TBP atmosphere until reaching a temperature below 300 °C.

Structural Characterization. The structural quality of individual crystals was investigated by scanning transmission electron microscopy (STEM) along the [-110] zone axis. The sample lamellas were prepared by means of a FEI Helios Nanolab 450S focused ion beam either in parallel to the growth direction for films grown along ⟨110⟩ or rotated by 45° for crystals grown along ⟨100⟩. BF and HAADF micrographs were generated using a double spherical aberration-corrected JEOL JEM-ARM200F microscope operated at 200 kV.

Optical Characterization. For optical characterization, crystals were transferred from their growth substrate to a piece of polystyrene (PS) after stripping the SiO_2 templates with BHF. Two different μ-PL setups were employed. At RT, a continuous laser source at 633 nm was used to excite the InP layers in ambient conditions, whereas for measurements at 5 K the crystals were pumped using a pulsed supercontinuum laser at 640 nm (pulse length 15 ps at 78 MHz repetition rate) in vacuum. Both setups, RT and low T, excite, as well as collect the photoluminescent response from the top using a 50× objective and they are linked to a liquid nitrogen-cooled Si CCD and InGaAs detector, respectively. TRPL measurements are performed at 5 K using the supercontinuum laser at 640 nm and 78 MHz, as well as a cooled InGaAs single-photon detector.

AUTHOR INFORMATION

Corresponding Author

*E-mail: sih@zurich.ibm.com.

ORCID

Philipp Staudinger: 0000-0003-3377-8575

Heinz Schmid: 0000-0002-0228-4268

Author Contributions

P.S. and H.S. conceived and designed the experiments. P.S. carried out template fabrication, MOCVD growth, STEM investigations and optical characterization at room temperature. H.S. prepared the TEM lamellas. PL and TRPL measurements at 5 K were done by S.M. All authors analyzed and discussed the results. The manuscript was written by P.S. and H.S. with contributions of all authors, and all authors have given approval to the final version of the manuscript.

Notes

The authors declare no competing financial interest.

ACKNOWLEDGMENTS

The authors gratefully acknowledge Antonis Olziersky, Marilyne Sousa, Yannick Baumgartner, Lukas Czornomaz, Emanuel Lörtscher, Anna Fontcuberta i Morral, Heike Riel, and Walter Riess. The work presented here has received funding from the European Union H2020 program SiLAS (Grant Agreement No. 735008), the ERC Starting Grant project PLASMIC (Grant Agreement No. 678567) and the Swiss National Science Foundation under Project Number 200021_156746.

REFERENCES

(1) Chau, R.; Datta, S.; Majumdar, A. Opportunities and Challenges of III-V Nanoelectronics for Future High-Speed, Low-Power Logic Applications. *Technol. Dig. - IEEE Compd. Semicond. Integr. Circuit Symp. CSIC* **2005**, 17−17.

(2) Joyce, H. J.; Gao, Q.; Hoe Tan, H.; Jagadish, C.; Kim, Y.; Zou, J.; Smith, L. M.; Jackson, H. E.; Yarrison-Rice, J. M.; Parkinson, P.; et al. III-V Semiconductor Nanowires for Optoelectronic Device Applications. *Prog. Quantum Electron.* **2011**, *35* (2−3), 23−75.

(3) Bett, a. W.; Dimroth, F.; Stollwerck, G.; Sulima, O. V. III-V Compounds for Solar Cell Applications. *Appl. Phys. A: Mater. Sci. Process.* **1999**, *69* (2), 119−129.

(4) Kitauchi, Y.; Kobayashi, Y.; Tomioka, K.; Hara, S.; Hiruma, K.; Fukui, T.; Motohisa, J. Structural Transition in Indium Phosphide Nanowires. *Nano Lett.* **2010**, *10* (5), 1699−1703.

(5) Woo, R. L.; Xiao, R.; Kobayashi, Y.; Gao, L.; Goel, N.; Hudait, M. K.; Mallouk, T. E.; Hicks, R. F. Effect of Twinning on the Photoluminescence and Photoelectrochemical Properties of Indium Phosphide Nanowires Grown on Silicon (111). *Nano Lett.* **2008**, *8*, 4664−4669.

(6) Perera, S.; Fickenscher, M. A.; Jackson, H. E.; Smith, L. M.; Yarrison-Rice, J. M.; Joyce, H. J.; Gao, Q.; Tan, H. H.; Jagadish, C.; Zhang, X.; et al. Nearly Intrinsic Exciton Lifetimes in Single Twin-Free GaAsAlGaAs Core-Shell Nanowire Heterostructures. *Appl. Phys. Lett.* **2008**, *93* (5), 053110.

(7) Parkinson, P.; Joyce, H. J.; Gao, Q.; Tan, H. H.; Zhang, X.; Zou, J.; Jagadish, C.; Herz, L. M.; Johnston, M. B. Carrier Lifetime and Mobility Enhancement in Nearly Defect-Free Core- Shell Nanowires Measured Using Time-Resolved Terahertz Spectroscopy. *Nano Lett.* **2009**, *9* (9), 3349−3353.

(8) De, A.; Pryor, C. E. Predicted Band Structures of III-V Semiconductors in the Wurtzite Phase. *Phys. Rev. B: Condens. Matter Mater. Phys.* **2010**, *81* (15), 155210.

(9) Zhang, L.; Luo, J. W.; Zunger, A.; Akopian, N.; Zwiller, V.; Harmand, J. C. Wide InP Nanowires with Wurtzite/Zincblende Superlattice Segments Are Type-II Whereas Narrower Nanowires Become Type-I: An Atomistic Pseudopotential Calculation. *Nano Lett.* **2010**, *10* (10), 4055−4060.

(10) Ikejiri, K.; Kitauchi, Y.; Tomioka, K.; Motohisa, J.; Fukui, T. Zinc Blende and Wurtzite Crystal Phase Mixing and Transition in Indium Phosphide Nanowires. *Nano Lett.* **2011**, *11* (10), 4314−4318.

(11) Gao, Q.; Saxena, D.; Wang, F.; Fu, L.; Mokkapati, S.; Guo, Y.; Li, L.; Wong-Leung, J.; Caroff, P.; Tan, H. H.; et al. Selective-Area Epitaxy of Pure Wurtzite InP Nanowires: High Quantum Efficiency and Room-Temperature Lasing. *Nano Lett.* **2014**, *14* (9), 5206−5211.

(12) Li, K.; Ng, K. W.; Tran, T.-T. D.; Sun, H.; Lu, F.; Chang-Hasnain, C. J. Wurtzite-Phased InP Micropillars Grown on Silicon with Low Surface Recombination Velocity. *Nano Lett.* **2015**, *15* (11), 7189−7198.

(13) Li, K.; Sun, H.; Ren, F.; Ng, K. W.; Tran, T.-T. D.; Chen, R.; Chang-Hasnain, C. J. Tailoring the Optical Characteristics of Microsized InP Nanoneedles Directly Grown on Silicon. *Nano Lett.* **2014**, *14* (1), 183−190.

(14) Spirkoska, D.; Arbiol, J.; Gustafsson, A.; Conesa-Boj, S.; Glas, F.; Zardo, I.; Heigoldt, M.; Gass, M. H.; Bleloch, A. L.; Estrade, S.; et al. Structural and Optical Properties of High Quality Zinc-Blende/

DOI: 10.1021/acs.nanolett.8b03632
Nano Lett. 2018, 18, 7856−7862

Wurtzite GaAs Nanowire Heterostructures. *Phys. Rev. B: Condens. Matter Mater. Phys.* **2009**, *80* (24), 1−9.
(15) Assali, S.; Zardo, I.; Plissard, S.; Kriegner, D.; Verheijen, M. A.; Bauer, G.; Meijerink, A.; Belabbes, A.; Bechstedt, F.; Haverkort, J. E. M.; et al. Direct Band Gap Wurtzite Gallium Phosphide Nanowires. *Nano Lett.* **2013**, *13* (4), 1559−1563.
(16) Wang, S. Q.; Ye, H. Q.; Search, H.; Journals, C.; Contact, A.; Iopscience, M.; Address, I. P. First-Principles Study on the Lonsdaleite Phases of C, Si and Ge. *J. Phys.: Condens. Matter* **2003**, *15* (12), L197.
(17) Gagliano, L.; Kruijsse, M.; Schefold, J. D. D.; Belabbes, A.; Verheijen, M. A.; Meuret, S.; Koelling, S.; Polman, A.; Bechstedt, F.; Haverkort, J. E. M.; Bakkers, E. P. A. M. Efficient Green Emission from Wurtzite $Al_xIn_{1-x}P$ Nanowires. *Nano Lett.* **2018**, *18* (6), 3543−3549.
(18) Hauge, H. I. T.; Conesa-Boj, S.; Verheijen, M. A.; Koelling, S.; Bakkers, E. P. A. M. Single-Crystalline Hexagonal Silicon−Germanium. *Nano Lett.* **2017**, *17* (1), 85−90.
(19) Shin, J. C.; Kim, K. H.; Yu, K. J.; Hu, H.; Yin, L.; Ning, C.-Z.; Rogers, J. A.; Zuo, J.-M.; Li, X. $In_xGa_{1-x}As$ Nanowires on Silicon: One-Dimensional Heterogeneous Epitaxy, Bandgap Engineering, and Photovoltaics. *Nano Lett.* **2011**, *11* (11), 4831−4838.
(20) Dick, K. A.; Caroff, P.; Bolinsson, J.; Messing, M. E.; Johansson, J.; Deppert, K.; Wallenberg, L. R.; Samuelson, L. Control of III−V Nanowire Crystal Structure by Growth Parameter Tuning. *Semicond. Sci. Technol.* **2010**, *25* (2), 024009.
(21) Knoedler, M.; Bologna, N.; Schmid, H.; Borg, M.; Moselund, K. E.; Wirths, S.; Rossell, M. D.; Riel, H. Observation of Twin-Free GaAs Nanowire Growth Using Template- Assisted Selective Epitaxy. *Cryst. Growth Des.* **2017**, *17* (12), 6297−6302.
(22) Wagner, R. S.; Ellis, W. C. Vapor-Liquid-Solid Mechanism of Single Crystal Growth. *Appl. Phys. Lett.* **1964**, *4* (5), 89−90.
(23) Tidemand-Petersson, P.; Albrektsen, O.; Salzman, J. Selective-Area MOVPE for InP-Based Optoelectronic Components. *Phys. Scr.* **1994**, *1994* (T54), 194.
(24) Schmid, H.; Borg, M.; Moselund, K.; Gignac, L.; Breslin, C. M.; Bruley, J.; Cutaia, D.; Riel, H. Template-Assisted Selective Epitaxy of III−V Nanoscale Devices for Co-Planar Heterogeneous Integration with Si. *Appl. Phys. Lett.* **2015**, *106* (23), 233101.
(25) Ogura, A.; Fujimoto, Y. Novel Technique for Si Epitaxial Lateral Overgrowth: Tunnel Epitaxy. *Appl. Phys. Lett.* **1989**, *55* (21), 2205−2207.
(26) Schubert, P. J.; Neudeck, G. W. Confined Lateral Selective Epitaxial Growth of Silicon for Device\nfabrication. *IEEE Electron Device Lett.* **1990**, *11* (5), 181−183.
(27) Pribat, D.; Karapiperis, L.; Collet, C. Conformal Vapor Phase Epitaxy. *Appl. Phys. Lett.* **1989**, *55* (24), 2544−2546.
(28) Joyce, H. J.; Wong-Leung, J.; Gao, Q.; Hoe Tan, H.; Jagadish, C. Phase Perfection in Zinc Blende and Wurtzite III- V Nanowires Using Basic Growth Parameters. *Nano Lett.* **2010**, *10* (3), 908−915.
(29) Mohan, P.; Motohisa, J.; Fukui, T. Controlled Growth of Highly Uniform, Axial/Radial Direction-Defined, Individually Addressable InP Nanowire Arrays. *Nanotechnology* **2005**, *16* (12), 2903−2907.
(30) Akiyama, T.; Nakamura, K.; Ito, T. Structural Stability and Electronic Structures of InP Nanowires: Role of Surface Dangling Bonds on Nanowire Facets. *Phys. Rev. B: Condens. Matter Mater. Phys.* **2006**, *73* (23), 235308.
(31) Wilhelm, C.; Larrue, A.; Dai, X.; Migas, D.; Soci, C. Anisotropic Photonic Properties of III-V Nanowires in the Zinc-Blende and Wurtzite Phase. *Nanoscale* **2012**, *4* (5), 1446−1454.
(32) Ishizaka, F.; Hiraya, Y.; Tomioka, K.; Fukui, T. Growth of Wurtzite GaP in InP/GaP Core−shell Nanowires by Selective-Area MOVPE. *J. Cryst. Growth* **2015**, *411*, 71−75.
(33) Algra, R. E.; Verheijen, M. A.; Borgström, M. T.; Feiner, L. F.; Immink, G.; Van Enckevort, W. J. P.; Vlieg, E.; Bakkers, E. P. A. M. Twinning Superlattices in Indium Phosphide Nanowires. *Nature* **2008**, *456* (7220), 369−372.
(34) Burgess, T.; Breuer, S.; Caroff, P.; Wong-Leung, J.; Gao, Q.; Hoe Tan, H.; Jagadish, C. Twinning Superlattice Formation in GaAs Nanowires. *ACS Nano* **2013**, *7* (9), 8105−8114.
(35) Glas, F.; Harmand, J. C.; Patriarche, G. Why Does Wurtzite Form in Nanowires of III-V Zinc Blende Semiconductors? *Phys. Rev. Lett.* **2007**, *99* (14), 3−6.
(36) Akiyama, T.; Sano, K.; Nakamura, K.; Ito, T. An Empirical Potential Approach to Wurtzite-Zinc-Blende Polytypism in Group III-V Semiconductor Nanowires. *Japanese J. Appl. Physics, Part 2 Lett.* **2006**, *45* (9), 1275−1278.
(37) Akiyama, T.; Kondo, T.; Tatematsu, H.; Nakamura, K.; Ito, T. Ab Initio Approach to Reconstructions of the InP(111)A Surface: Role of Hydrogen Atoms Passivating Surface Dangling Bonds. *Phys. Rev. B: Condens. Matter Mater. Phys.* **2008**, *78* (20), 1−7.
(38) Li, H.; Sun, Y.; Law, C.; Visbeck, B.; Hicks, F. Reconstructions of the InP(111)A Surface. *Phys. Rev. B: Condens. Matter Mater. Phys.* **2003**, *68* (8), 1−5.

DOI: 10.1021/acs.nanolett.8b03632
Nano Lett. 2018, 18, 7856−7862

NANO LETTERS

Letter

Cite This: Nano Lett. 2018, 18, 7856−7862

pubs.acs.org/NanoLett

Concurrent Zinc-Blende and Wurtzite Film Formation by Selection of Confined Growth Planes

Philipp Staudinger, Svenja Mauthe, Kirsten E. Moselund, and Heinz Schmid*

IBM Research - Zürich, Säumerstrasse 4, 8803 Rüschlikon, Switzerland

ABSTRACT: Recent research on nanowires (NWs) demonstrated the ability of III−V semiconductors to adopt a different crystallographic phase when they are grown as nanostructures, giving rise to a novel class of materials with unique properties. Controlling the crystal structure however remains difficult and the geometrical constraints of NWs cause integration challenges for advanced devices. Here, we report for the first time on the phase-controlled growth of micron-sized planar InP films by selecting confined growth planes during template-assisted selective epitaxy. We demonstrate this by varying the orientation of predefined templates, which results in concurrent formation of zinc-blende (ZB) and wurtzite (WZ) material exhibiting phase purities of 100% and 97%, respectively. Optical characterization revealed a 70 meV higher band gap and a 2.5× lower lifetime for WZ InP in comparison to its natural ZB phase. Further, a model for the transition of the crystal structure is presented based on the observed growth facets and the bonding configuration of InP surfaces.

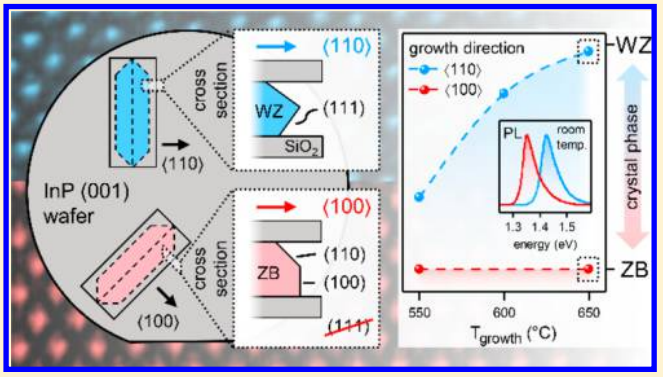

KEYWORDS: *Crystal structure, zinc-blende, wurtzite, indium phosphide, template-assisted selective epitaxy*

Group III−V semiconductor nanostructures are key components for high-speed electronic,[1] optoelectronic,[2] and photovoltaic[3] applications due to their favorable material properties and the flexibility to employ various kinds of heterostructures.[4] One of the main challenges is the formation of high-quality material, because nanostructures and in particular grown NWs typically suffer from high densities of planar defects (PDs) such as rotational twins and stacking faults. PDs lead to lower performance by reducing quantum efficiency, carrier lifetime, and mobility as well as introducing nonradiative recombination centers and scattering planes.[5−7] Moreover, the control of the crystal phase is of key importance because, for example, for InP it has been reported both theoretically[8,9] and experimentally[10,11] that the band structure varies significantly between the cubic ZB and the related hexagonal WZ structure resulting in a bandgap energy difference of about 70 meV and type-II superlattices if they are intermixed.[12,13] While it is obvious that uncontrolled polytypism limits the opportunities for applications, the possibility to selectively tune electronic and optical properties within the same material system by crystal phase engineering results in a unique degree of freedom for enhancing the functionality of emerging devices. Spirkoska et al. demonstrated the spatial carrier confinement in quantum-well structures formed by ZB/WZ heterostructures in GaAs,[14] whereas other materials such as GaP, AlP, and Ge even change the bandgap from indirect to direct when the crystal structure is converted from cubic to hexagonal.[8,15,16] These findings recently enabled efficient emission in the amber-green region of the visible spectrum from AlInP NWs[17] and may pave the way toward SiGe light sources with a bandgap close to the telecommunication wavelength.[18] So far, however, the crystal phase remains challenging to control and phase intermixing is a commonly observed problem for III−V integration.[19−21] In addition, the two most explored techniques, vapor−liquid−solid (VLS)[22] and selective area growth,[23] cannot surmount the size constraints of NWs with diameters below a few hundreds of nanometers causing fundamental challenges for device integration which is conventionally based on planar structures.

In this study, we report on micron-sized InP layers epitaxially deposited inside hollow SiO_2 cavities on top of an InP(001) substrate. We demonstrate that the crystal structure can be controlled by confining and guiding the growth along specific crystalline directions, namely ⟨100⟩ and ⟨110⟩ for ZB and WZ, respectively. Thus, we achieve simultaneous formation of planar films exhibiting both crystal phases at sizes up to 50 μm^2. Crystal structure and defects are characterized by scanning transmission electron microscopy (STEM) along with microphotoluminescence (μ-PL) measurements and are found to be pure and without defects for ZB and with a stacking-purity of about 97% for WZ crystals. This is the first report demonstrating the fabrication of micron-sized WZ InP layers, thus opening new pathways for exploring fundamental material properties as well as establishing novel

Received: September 7, 2018
Revised: October 29, 2018
Published: November 14, 2018

DOI: 10.1021/acs.nanolett.8b03632
Nano Lett. 2018, 18, 7856−7862

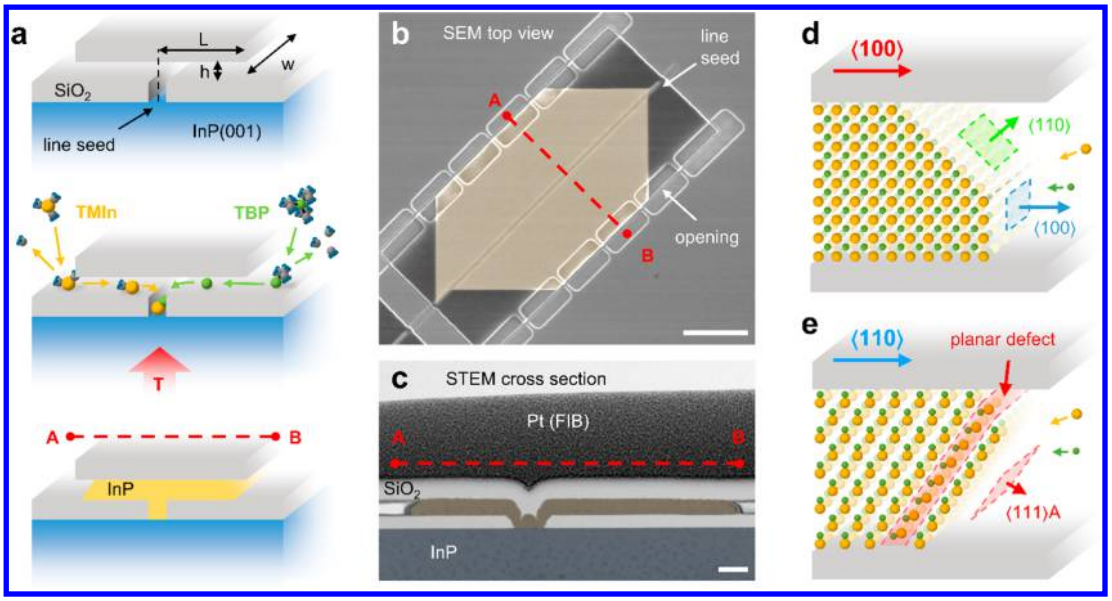

Figure 1. Experimental implementation of confined growth planes. (a) From top to bottom: empty SiO_2 cavity as processed on top of an InP(001) substrate, sketch of the selective epitaxy process, and template after MOCVD growth. (b) SEM top view image of an InP crystal after growth (colored in yellow). The crystal expands from the central line seed toward the openings. Scale bar: 1 μm. (c) Low-resolution BF-STEM image showing the cross section of a crystal (yellow) on top of the InP(001) substrate (blue). Scale bar: 100 nm. (d,e) Illustrations to show faceting along different growth orientations. {111} facets and therefore PDs can only be formed when the crystals are grown along ⟨110⟩.

devices. Although InP was used as a model system, to some extent these findings are expected to be valid also for other compound semiconductor materials.

To grow InP films on InP(001), we employ a method similar to template-assisted selective epitaxy (TASE)[24] but using much larger and elongated seed areas as reported in tunnel epitaxy,[25] confined lateral selective epitaxial growth,[26] or conformal vapor phase epitaxy.[27] In essence, we pattern line seeds on top of SiO_2 covered InP(001) substrates, which are aligned along various crystalline orientations and capped again with an SiO_2 layer (Figure 1a top). Selective epitaxy of InP is carried out in an MOCVD reactor using trimethylindium (TMIn) and tertiarybutylphosphine (TBP) at a V/III precursor ratio of 100 and variable temperatures (T_{growth}) until the templates (L = 1 μm) are filled (Figure 1a bottom). Growth rates are in the range of 0.5−1 μm/h depending on reactor conditions with excellent selectivity to the SiO_2 cavity. See Methods for more details on the process. An SEM top view micrograph of a typical crystal exhibiting a width w = 5 μm is depicted in Figure 1b. Clear faceting demonstrates the homoepitaxial and single-crystalline nature of the deposition process and was observed irrespective of template width up to 50 μm (the widest investigated in this study). A cross sectional low-resolution bright field (BF)-STEM image of another crystal is shown in Figure 1c.

To demonstrate the effect of confined growth planes we compare films grown from two different template orientations. In the first case the line seed is oriented along ⟨100⟩ and the crystals thus grow along another ⟨100⟩ direction perpendicular to it (Figure 1d). Given that there is a single growth front in parallel to the seed line, which is typically observed in our experiments (compare Figure 1b), the local growth direction must lie within the plane perpendicular to this seed line. Low order facets in this direction include {100} and {110}, but notably no {111} facets along which PDs could be formed. Thus, we expect pure ZB phase for crystals grown along this direction.[21] InP grown along a ⟨110⟩ orientation in contrast allows for different faceting, since both ⟨111⟩A and ⟨111⟩B directions are available locally and hence we expect to obtain PDs as indicated in Figure 1e. In the second case, controlling the stacking sequence would yield the possibility to transform the crystal phase from ZB (ABC stacking) to other polytypes such as the WZ structure (ABAB stacking).

First, we characterize crystals grown along the ⟨100⟩ direction using STEM. Figure 2a depicts a representative high-angle annular dark field (HAADF) image of a film grown at standard conditions for InP growth (T_{growth} = 550 °C, V/III = 100). Note that the zone axis is [−110] and thus not

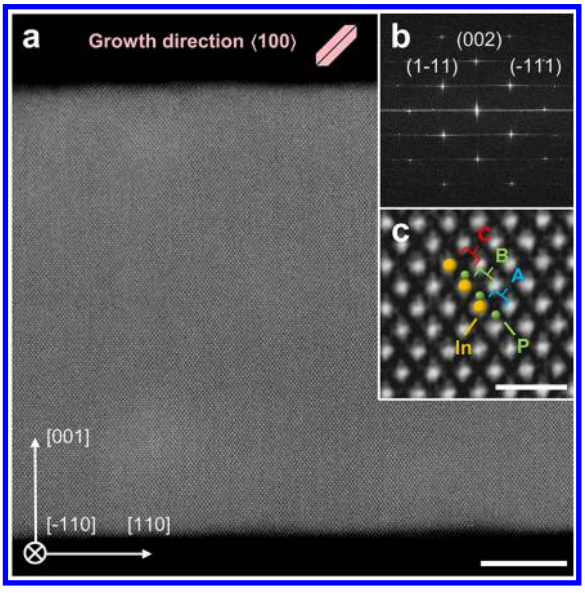

Figure 2. STEM investigation of an InP crystal grown along ⟨100⟩. (a) Cross-sectional overview of the film with height h = 50 nm. Scale bar: 10 nm. (b) Corresponding FFT pattern showing ZB symmetry. (c) HR-image demonstrating the ABC type stacking. Scale bar: 1 nm.

DOI: 10.1021/acs.nanolett.8b03632
Nano Lett. 2018, 18, 7856−7862

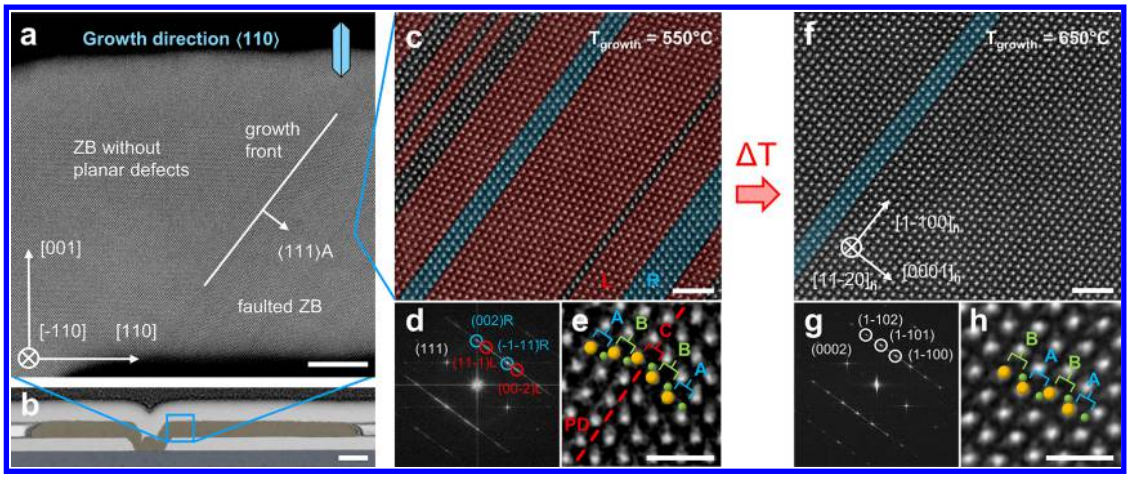

Figure 3. STEM investigation of InP films grown along ⟨110⟩. (a,b) Cross-sectional overview of the crystal with height h = 50 nm close to the seed area. Scale bars: 10 and 100 nm. (c,f) HR-STEM images of InP crystals grown at 550 and 650 °C, respectively. Colored areas represent ZB segments with the two possible stacking orientations (ABC, CBA). Scale bars: 2 nm. (d,f) Corresponding FFT patterns showing faulted ZB and WZ symmetry, respectively. (e,h) Detailed micrographs of the crystal stacking. Scale bars: 1 nm.

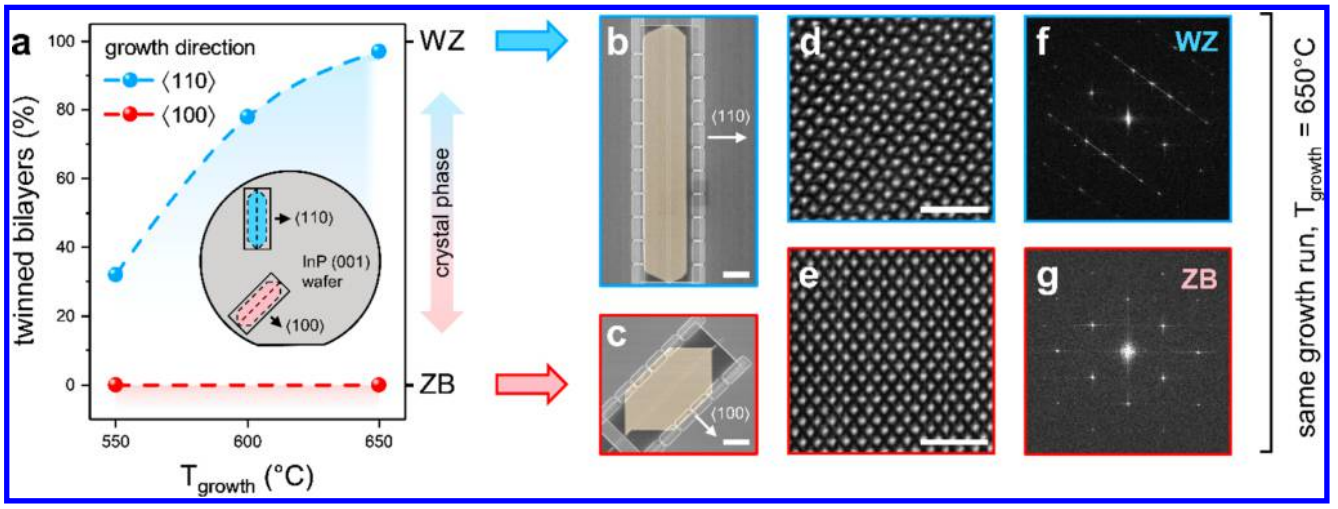

Figure 4. Simultaneous growth of ZB and WZ InP layers. (a) Number of twinned bilayers as a function of growth temperature for InP films grown along ⟨110⟩ and ⟨100⟩. Simultaneous formation is achieved at 650 °C. (b,c) Colored top-view SEM images of typical crystals. Scale bars: 1 μm. (d,e) HR-STEM images of InP crystals grown along ⟨110⟩ and ⟨100⟩, respectively. Scale bars: 2 nm. (f,g) Corresponding FFT patterns showing WZ and ZB symmetry, respectively.

perpendicular to the growing direction but rotated by 45°. The entire cross-section of the h = 50 nm high film is shown in this image. We have not found any defects along the entire crystal and thus pure ZB phase is obtained, which is attributed to the specific growth geometry and the related absence of {111} facets. Figure 2b,c depict the corresponding fast Fourier transform (FFT) pattern as well as a high-resolution (HR)-STEM image showing the ABC type ZB stacking.

Similarly, an InP film grown with identical conditions but along the ⟨110⟩ direction is shown in Figure 3a–e. First, we investigate the area close to the beginning of the growth as seen from the [−110] zone axis indicated in the BF-STEM micrograph in Figure 3b. We typically observe pure ZB InP without PDs for the first few tens of nanometers (Figure 3a) but as soon as the first PD occurs we immediately obtain a high defect density (~1 PD/nm), as it is depicted in more detail in Figure 3c. We therefore conclude that the crystal as it is expanding from the horizontal substrate follows growth directions deviating from ⟨111⟩ in the beginning, however as soon as the (111)A facet is present it remains stable and PDs can be formed easily due to its high susceptibility to twinning. The presence of these PDs also manifests itself in the corresponding FFT pattern presented in Figure 3d. A single rotational twin and the related inversion of the stacking sequence is depicted in Figure 3e in more detail. In a second experiment, the growth temperature is increased by 100 °C to T_{growth} = 650 °C by ramping up from 600 °C within the first 5 min to prevent desorption of the otherwise unstable InP (001) surface under the growth conditions accessible in our MOCVD reactor. As shown in Figures 3f the number of ZB segments is reduced strongly. Although only a small area is shown in this image, we observe similar crystal quality and defect density throughout the entire template, apart from the area close to the seed. The characteristic FFT pattern and ABAB stacking sequence along the $[0001]_h$ direction are clearly visible in Figure 3g,h demonstrating the formation of nearly pure WZ material. At the beginning of the growth, we obtain pure ZB material again, followed by a short polytypic region (~20 nm), which we believe originates from the temperature ramping procedure.

DOI: 10.1021/acs.nanolett.8b03632
Nano Lett. 2018, 18, 7856−7862

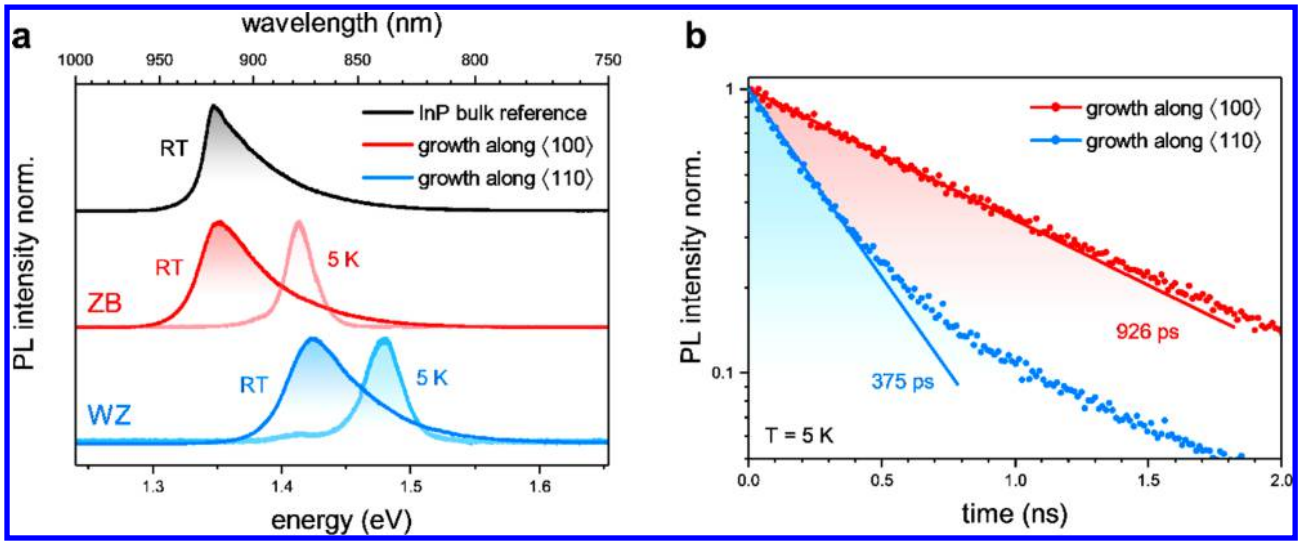

Figure 5. PL measurements of ZB and WZ InP films. (a) Normalized emission spectra of typical crystals along with bulk InP(001) at RT as well as 5 K. (b) Normalized TRPL measurements at 5 K demonstrate lifetime differences of ZB and WZ InP crystals exhibiting the exact same morphology.

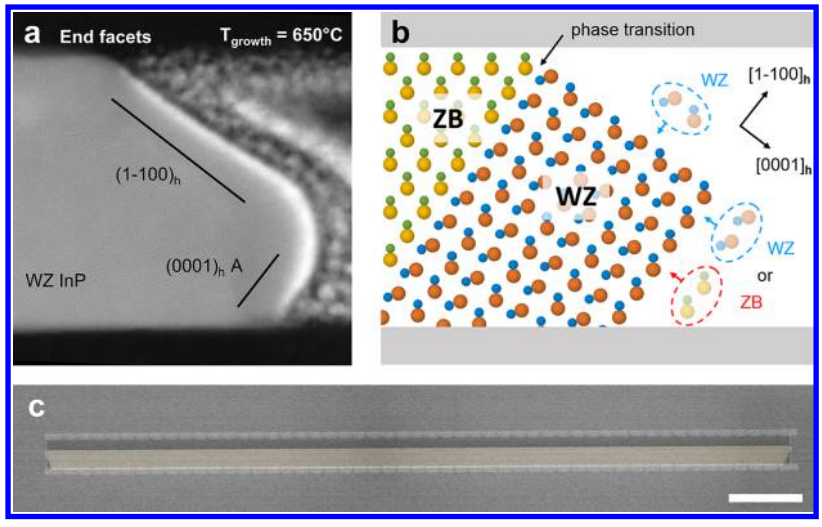

Figure 6. (a) End facets of a typical InP film grown in ⟨110⟩ direction and exhibiting WZ phase. (b) Atomistic model for structural transition in InP crystals. The variable stacking axis along the $[0001]_h$ A direction allows for an initial phase transition, which needs to be maintained during growth by forming nuclei at the edge toward the $(1\text{-}100)_h$ facet. In $[1\text{-}100]_h$ direction the stacking is strongly fixed and the WZ structure is transferred irrespective of growth conditions. (c) WZ InP film exhibiting a width w = 50 μm and a length L = 1 μm demonstrating the scalability of this approach. Scale bar: 5 μm.

We use statistical analysis proposed by Joyce et al.[28] to quantify the crystalline purity of our InP films. Every deviation from the perfect ZB stacking order (ABC) is accounted for as a single twinned bilayer (e.g. AB$\underline{A}$). As the proportion of twinned bilayers in ZB InP is increased from 0 to 100%, the crystal phase is thus transferred to pure WZ. In Figure 4a, we employ this analysis for different growth temperatures and directions by counting PDs in HR-STEM images. We observe that the number of twinned bilayers increases with temperature from 32% to 97% for films grown along ⟨110⟩ to nearly pure WZ at 650 °C. InP grown in ⟨100⟩-direction on the other hand remains free of PDs and is pure ZB in any case. Hence, we achieve simultaneous formation of both phases during the same growth run as demonstrated in Figure 4b–g. Increasing the temperature further is expected to result in even higher phase purity, however the TBP pressure in our MOCVD reactor was not sufficient to stabilize the InP surface under such conditions.

To further confirm the crystal phase transition and purity, we perform μ-PL on individual crystals after removal from the underlying InP substrate to exclude measurement interferences (see Methods for more details). Figure 5a depicts representative μ-PL emission spectra of InP crystals grown along ⟨100⟩ and ⟨110⟩ respectively, as well as of bulk InP as a reference. The PL measurements reveal a blueshift of about 70 meV for crystals grown along ⟨110⟩ with respect to bulk InP and crystals grown along the ⟨100⟩ direction. This shift, which is clearly observed for room temperature (RT) and low T measurements, is thus attributed to the phase change of the material. For WZ InP, we extract band gap energies corresponding to 1.41 and 1.47 eV for 293 and 5 K, respectively, which is in excellent agreement with previous reports on WZ InP NWs.[12,29] Additionally, at low T we obtain

DOI: 10.1021/acs.nanolett.8b03632
Nano Lett. 2018, 18, 7856−7862

a much smaller emission peak exactly at the position of bulk InP. This is believed to be due to the area close to the seed line which is ZB irrespective of template orientation. The fwhm of the spontaneous emission peaks for crystals grown along ⟨100⟩ and ⟨110⟩ is comparable to the one measured for bulk InP indicating high material quality and phase purity. Further, we use time-resolved PL (TRPL) to assess the overall effective carrier lifetime in our InP films. In Figure 5b we compare TRPL-measurements performed at 5 K from two crystals obtained during the same growth run and having the same defined morphology, the only difference being the growth direction and thus crystal phase. We obtain a 2.5-fold longer lifetime for ZB InP. According to the equivalent crystal morphology and assuming that there is no fundamental difference between the quality of the WZ and ZB InP surfaces, we thus conclude that the shorter exciton recombination lifetimes are an inherent property of the crystal phase and reflect the increased oscillator strength of the optical transition at the Γ-point.[30,31] These findings suggest the enhanced light emission from WZ InP as compared to its natural ZB crystal structure, which could result in more efficient light sources.

Next, we describe a model to explain the structural transition observed in crystals grown along the ⟨110⟩ direction. It is crucial to understand which type of facets are formed during the deposition process as they have a substantial influence on the growth dynamics. For example, PDs, which are essential to facilitate a phase transition, are exclusively formed along either the ZB ⟨111⟩A or ⟨111⟩B direction. In Figure 6a, we show the end facets of a typical WZ InP film, which consist out of a relatively small $(0001)_h$ A facet at the bottom and a larger $(1\text{-}100)_h$ facet perpendicular to it. As sketched in Figure 6b, the stacking sequence can easily be changed along the $\langle 0001\rangle_h$ direction which corresponds to the ⟨111⟩ direction in ZB. Hence, a transition from ZB to WZ is possible without introducing miscoordinated atoms.[32]

The question remains, why under certain conditions WZ stacking is preferred over ZB, which is known to be more stable in bulk form. Earlier experiments on vapor−liquid−solid (VLS) grown NWs suggest that once a nucleus of critical size is formed it spreads out laterally over the entire surface resulting in a layer-by-layer deposition mechanism.[33,34] The orientation of the initial nuclei for every layer therefore determines the stacking sequence and thus the crystal phase of the resulting material. It is further known from VLS growth that if such a nucleus is formed at the edge to the $(1\text{-}100)_h$ facet, WZ is preferred to minimize the overall surface energy, otherwise ZB stacking is energetically more favorable under typical growth conditions.[35,36] Hence, it is important to control the position of the nuclei on the $(0001)_h$ A surface to achieve control over the crystal phase.

Keeping this information in mind, we can have a closer look at the InP (111)A/$(0001)_h$ A surface. It is reported both theoretically[37] and experimentally[38] that its surface reconstruction is either In-rich (2 × 2) or P-rich (3 × 3)$R30°$ depending on growth temperature and precursor partial pressures. In the former case, which is at high T_{growth},[37] to proceed growth on the In-terminated surface, P atoms need to be adsorbed first. However, this bonding configuration is thought to be weak since it has only a single bond toward the surface, and the P atoms are desorbed easily.[4] We thus speculate that under such conditions the formation of nuclei exceeding the critical size becomes unlikely at the surface. Instead new layers start to form at the edge toward the $(1\text{-}100)_h$ facet where a high amount of dangling bonds is available and WZ phase is preferred in analogy to the existing models for the much more explored VLS technique.[35] This model can explain how the WZ phase becomes more dominant at higher T_{growth}, because the direct nucleation at the surface is suppressed and new nuclei are forced to be formed at the edge line. This is also in agreement with the fact that we observe a decrease of the growth rate when T_{growth} is increased from 550 to 650 °C.

Our model suggests that a low ratio between the $(0001)_h$A surface and its accompanying edge to the neighboring $(1\text{-}100)_h$ facet is required to prevent ZB nucleation on the $(0001)_h$A surface. Because in NW growth this ratio scales with diameter, stable WZ formation has not been observed in NWs exceeding a few hundred nanometers, nor in any planar epitaxy. For the same reason, increasing the height (h) of InP films grown by TASE is expected to result in polytypic material at a certain point. However, this ratio is constant irrespective of another parameter in our constrained geometry: the template width (w). We do not believe that there is any restriction to this value, which would enable the growth of arbitrarily wide crystals in a planar way. This was demonstrated by growing WZ films exhibiting an area of 50 μm^2, as shown in Figure 6c. Using such planar films as virtual substrates by subsequently transferring the crystal phase in vertical direction holds great promise for integrating more complex WZ thin-film heterostructures, perfectly suited for electro-optical devices.

In conclusion, by carefully selecting confined growth planes using TASE, we achieved the concurrent growth of pure ZB and nearly pure WZ InP films. Thus, we demonstrated a new pathway for facilitating complete phase transitions in a III−V material system. STEM, FFT, and PL analysis revealed the phase purity and optical quality of the obtained crystals and demonstrated a blueshift for the WZ phase in agreement with earlier literature reports on WZ InP NWs. By TRPL measurements, we obtained lower exciton lifetimes in the WZ phase which is a strong indicator for the increased oscillator strength of the optical transition and the resulting enhanced light emission of the material. We further proposed a model to describe our findings and demonstrated the scalability of our approach by growing WZ InP at sizes up to 50 μm^2. Remarkably, the growth of WZ InP has only been demonstrated in NW structures with the first WZ film formation shown in this work. Our study provides a new route for facilitating phase transitions in large area III−V material growth, which could bring us one step closer to the integration of a new class of optical devices with outstanding properties.

METHODS

Template Fabrication. Line seeds with nominal widths of 50 nm were patterned along the ⟨100⟩ and ⟨110⟩ direction on a standard InP(001) wafer covered with 50 nm plasma-enhanced chemical vapor deposited (PECVD) SiO_2 by e-beam lithography (EBL), reactive ion etching (RIE), and buffered hydrofluoric acid (BHF). Seeds were protected with 4 nm atomic-layer deposited (ALD) Al_2O_3 after which 50 or 100 nm amorphous Si (α-Si) was sputtered for structural and optical characterization, respectively. Sacrificial structures were patterned perpendicular to the seed lines with varying widths and lengths using EBL, inductively coupled plasma (ICP)-RIE, and a short diluted HF (DHF) dip to remove the Al_2O_3 after which the actual 50 nm thick SiO_2 templates are deposited

DOI: 10.1021/acs.nanolett.8b03632
Nano Lett. 2018, 18, 7856−7862

using ALD. The SiO_2 is opened at the position furthest away from the seed line using EBL, RIE, and DHF, and the α-Si within is etched using XeF_2 chemistry. Finally, the protective Al_2O_3 at the seed line is removed by DHF directly before the growth.

InP Growth. InP film growth was performed by MOCVD using TBP and TMIn at a total pressure of 60 Torr. Partial pressures for TBP and TMIn were kept at 8.2 Pa and 82 mPa, respectively, to achieve a nominal V/III ratio of 100. Upon loading, the reactor was heated in a TBP atmosphere, and deposition was initiated subsequently by introducing TMIn. Growth temperature was held constant for growth at 550 and 600 °C and ramped up from 600 °C within the first 5 min for growth at 650 °C to prevent desorption of the thermally unstable InP(001) substrate surface at the seed line. Growth times were varied between 40 and 60 min. After growth, substrates were cooled under a TBP atmosphere until reaching a temperature below 300 °C.

Structural Characterization. The structural quality of individual crystals was investigated by scanning transmission electron microscopy (STEM) along the [-110] zone axis. The sample lamellas were prepared by means of a FEI Helios Nanolab 450S focused ion beam either in parallel to the growth direction for films grown along ⟨110⟩ or rotated by 45° for crystals grown along ⟨100⟩. BF and HAADF micrographs were generated using a double spherical aberration-corrected JEOL JEM-ARM200F microscope operated at 200 kV.

Optical Characterization. For optical characterization, crystals were transferred from their growth substrate to a piece of polystyrene (PS) after stripping the SiO_2 templates with BHF. Two different μ-PL setups were employed. At RT, a continuous laser source at 633 nm was used to excite the InP layers in ambient conditions, whereas for measurements at 5 K the crystals were pumped using a pulsed supercontinuum laser at 640 nm (pulse length 15 ps at 78 MHz repetition rate) in vacuum. Both setups, RT and low T, excite, as well as collect the photoluminescent response from the top using a 50× objective and they are linked to a liquid nitrogen-cooled Si CCD and InGaAs detector, respectively. TRPL measurements are performed at 5 K using the supercontinuum laser at 640 nm and 78 MHz, as well as a cooled InGaAs single-photon detector.

AUTHOR INFORMATION

Corresponding Author

*E-mail: sih@zurich.ibm.com.

ORCID

Philipp Staudinger: 0000-0003-3377-8575

Heinz Schmid: 0000-0002-0228-4268

Author Contributions

P.S. and H.S. conceived and designed the experiments. P.S. carried out template fabrication, MOCVD growth, STEM investigations and optical characterization at room temperature. H.S. prepared the TEM lamellas. PL and TRPL measurements at 5 K were done by S.M. All authors analyzed and discussed the results. The manuscript was written by P.S. and H.S. with contributions of all authors, and all authors have given approval to the final version of the manuscript.

Notes

The authors declare no competing financial interest.

ACKNOWLEDGMENTS

The authors gratefully acknowledge Antonis Olziersky, Marilyne Sousa, Yannick Baumgartner, Lukas Czornomaz, Emanuel Lörtscher, Anna Fontcuberta i Morral, Heike Riel, and Walter Riess. The work presented here has received funding from the European Union H2020 program SiLAS (Grant Agreement No. 735008), the ERC Starting Grant project PLASMIC (Grant Agreement No. 678567) and the Swiss National Science Foundation under Project Number 200021_156746.

REFERENCES

(1) Chau, R.; Datta, S.; Majumdar, A. Opportunities and Challenges of III-V Nanoelectronics for Future High-Speed, Low-Power Logic Applications. *Technol. Dig. - IEEE Compd. Semicond. Integr. Circuit Symp. CSIC* **2005**, 17−17.

(2) Joyce, H. J.; Gao, Q.; Hoe Tan, H.; Jagadish, C.; Kim, Y.; Zou, J.; Smith, L. M.; Jackson, H. E.; Yarrison-Rice, J. M.; Parkinson, P.; et al. III-V Semiconductor Nanowires for Optoelectronic Device Applications. *Prog. Quantum Electron.* **2011**, *35* (2−3), 23−75.

(3) Bett, a. W.; Dimroth, F.; Stollwerck, G.; Sulima, O. V. III-V Compounds for Solar Cell Applications. *Appl. Phys. A: Mater. Sci. Process.* **1999**, *69* (2), 119−129.

(4) Kitauchi, Y.; Kobayashi, Y.; Tomioka, K.; Hara, S.; Hiruma, K.; Fukui, T.; Motohisa, J. Structural Transition in Indium Phosphide Nanowires. *Nano Lett.* **2010**, *10* (5), 1699−1703.

(5) Woo, R. L.; Xiao, R.; Kobayashi, Y.; Gao, L.; Goel, N.; Hudait, M. K.; Mallouk, T. E.; Hicks, R. F. Effect of Twinning on the Photoluminescence and Photoelectrochemical Properties of Indium Phosphide Nanowires Grown on Silicon (111). *Nano Lett.* **2008**, *8*, 4664−4669.

(6) Perera, S.; Fickenscher, M. A.; Jackson, H. E.; Smith, L. M.; Yarrison-Rice, J. M.; Joyce, H. J.; Gao, Q.; Tan, H. H.; Jagadish, C.; Zhang, X.; et al. Nearly Intrinsic Exciton Lifetimes in Single Twin-Free GaAsAlGaAs Core-Shell Nanowire Heterostructures. *Appl. Phys. Lett.* **2008**, *93* (5), 053110.

(7) Parkinson, P.; Joyce, H. J.; Gao, Q.; Tan, H. H.; Zhang, X.; Zou, J.; Jagadish, C.; Herz, L. M.; Johnston, M. B. Carrier Lifetime and Mobility Enhancement in Nearly Defect-Free Core- Shell Nanowires Measured Using Time-Resolved Terahertz Spectroscopy. *Nano Lett.* **2009**, *9* (9), 3349−3353.

(8) De, A.; Pryor, C. E. Predicted Band Structures of III-V Semiconductors in the Wurtzite Phase. *Phys. Rev. B: Condens. Matter Mater. Phys.* **2010**, *81* (15), 155210.

(9) Zhang, L.; Luo, J. W.; Zunger, A.; Akopian, N.; Zwiller, V.; Harmand, J. C. Wide InP Nanowires with Wurtzite/Zincblende Superlattice Segments Are Type-II Whereas Narrower Nanowires Become Type-I: An Atomistic Pseudopotential Calculation. *Nano Lett.* **2010**, *10* (10), 4055−4060.

(10) Ikejiri, K.; Kitauchi, Y.; Tomioka, K.; Motohisa, J.; Fukui, T. Zinc Blende and Wurtzite Crystal Phase Mixing and Transition in Indium Phosphide Nanowires. *Nano Lett.* **2011**, *11* (10), 4314−4318.

(11) Gao, Q.; Saxena, D.; Wang, F.; Fu, L.; Mokkapati, S.; Guo, Y.; Li, L.; Wong-Leung, J.; Caroff, P.; Tan, H. H.; et al. Selective-Area Epitaxy of Pure Wurtzite InP Nanowires: High Quantum Efficiency and Room-Temperature Lasing. *Nano Lett.* **2014**, *14* (9), 5206−5211.

(12) Li, K.; Ng, K. W.; Tran, T.-T. D.; Sun, H.; Lu, F.; Chang-Hasnain, C. J. Wurtzite-Phased InP Micropillars Grown on Silicon with Low Surface Recombination Velocity. *Nano Lett.* **2015**, *15* (11), 7189−7198.

(13) Li, K.; Sun, H.; Ren, F.; Ng, K. W.; Tran, T.-T. D.; Chen, R.; Chang-Hasnain, C. J. Tailoring the Optical Characteristics of Microsized InP Nanoneedles Directly Grown on Silicon. *Nano Lett.* **2014**, *14* (1), 183−190.

(14) Spirkoska, D.; Arbiol, J.; Gustafsson, A.; Conesa-Boj, S.; Glas, F.; Zardo, I.; Heigoldt, M.; Gass, M. H.; Bleloch, A. L.; Estrade, S.; et al. Structural and Optical Properties of High Quality Zinc-Blende/

DOI: 10.1021/acs.nanolett.8b03632
Nano Lett. 2018, 18, 7856−7862

Wurtzite GaAs Nanowire Heterostructures. *Phys. Rev. B: Condens. Matter Mater. Phys.* **2009**, *80* (24), 1−9.
(15) Assali, S.; Zardo, I.; Plissard, S.; Kriegner, D.; Verheijen, M. A.; Bauer, G.; Meijerink, A.; Belabbes, A.; Bechstedt, F.; Haverkort, J. E. M.; et al. Direct Band Gap Wurtzite Gallium Phosphide Nanowires. *Nano Lett.* **2013**, *13* (4), 1559−1563.
(16) Wang, S. Q.; Ye, H. Q.; Search, H.; Journals, C.; Contact, A.; Iopscience, M.; Address, I. P. First-Principles Study on the Lonsdaleite Phases of C, Si and Ge. *J. Phys.: Condens. Matter* **2003**, *15* (12), L197.
(17) Gagliano, L.; Kruijsse, M.; Schefold, J. D. D.; Belabbes, A.; Verheijen, M. A.; Meuret, S.; Koelling, S.; Polman, A.; Bechstedt, F.; Haverkort, J. E. M.; Bakkers, E. P. A. M. Efficient Green Emission from Wurtzite $Al_xIn_{1-x}P$ Nanowires. *Nano Lett.* **2018**, *18* (6), 3543−3549.
(18) Hauge, H. I. T.; Conesa-Boj, S.; Verheijen, M. A.; Koelling, S.; Bakkers, E. P. A. M. Single-Crystalline Hexagonal Silicon−Germanium. *Nano Lett.* **2017**, *17* (1), 85−90.
(19) Shin, J. C.; Kim, K. H.; Yu, K. J.; Hu, H.; Yin, L.; Ning, C.-Z.; Rogers, J. A.; Zuo, J.-M.; Li, X. $In_xGa_{1-x}As$ Nanowires on Silicon: One-Dimensional Heterogeneous Epitaxy, Bandgap Engineering, and Photovoltaics. *Nano Lett.* **2011**, *11* (11), 4831−4838.
(20) Dick, K. A.; Caroff, P.; Bolinsson, J.; Messing, M. E.; Johansson, J.; Deppert, K.; Wallenberg, L. R.; Samuelson, L. Control of III−V Nanowire Crystal Structure by Growth Parameter Tuning. *Semicond. Sci. Technol.* **2010**, *25* (2), 024009.
(21) Knoedler, M.; Bologna, N.; Schmid, H.; Borg, M.; Moselund, K. E.; Wirths, S.; Rossell, M. D.; Riel, H. Observation of Twin-Free GaAs Nanowire Growth Using Template- Assisted Selective Epitaxy. *Cryst. Growth Des.* **2017**, *17* (12), 6297−6302.
(22) Wagner, R. S.; Ellis, W. C. Vapor-Liquid-Solid Mechanism of Single Crystal Growth. *Appl. Phys. Lett.* **1964**, *4* (5), 89−90.
(23) Tidemand-Petersson, P.; Albrektsen, O.; Salzman, J. Selective-Area MOVPE for InP-Based Optoelectronic Components. *Phys. Scr.* **1994**, *1994* (T54), 194.
(24) Schmid, H.; Borg, M.; Moselund, K.; Gignac, L.; Breslin, C. M.; Bruley, J.; Cutaia, D.; Riel, H. Template-Assisted Selective Epitaxy of III−V Nanoscale Devices for Co-Planar Heterogeneous Integration with Si. *Appl. Phys. Lett.* **2015**, *106* (23), 233101.
(25) Ogura, A.; Fujimoto, Y. Novel Technique for Si Epitaxial Lateral Overgrowth: Tunnel Epitaxy. *Appl. Phys. Lett.* **1989**, *55* (21), 2205−2207.
(26) Schubert, P. J.; Neudeck, G. W. Confined Lateral Selective Epitaxial Growth of Silicon for Device\nfabrication. *IEEE Electron Device Lett.* **1990**, *11* (5), 181−183.
(27) Pribat, D.; Karapiperis, L.; Collet, C. Conformal Vapor Phase Epitaxy. *Appl. Phys. Lett.* **1989**, *55* (24), 2544−2546.
(28) Joyce, H. J.; Wong-Leung, J.; Gao, Q.; Hoe Tan, H.; Jagadish, C. Phase Perfection in Zinc Blende and Wurtzite III- V Nanowires Using Basic Growth Parameters. *Nano Lett.* **2010**, *10* (3), 908−915.
(29) Mohan, P.; Motohisa, J.; Fukui, T. Controlled Growth of Highly Uniform, Axial/Radial Direction-Defined, Individually Addressable InP Nanowire Arrays. *Nanotechnology* **2005**, *16* (12), 2903−2907.
(30) Akiyama, T.; Nakamura, K.; Ito, T. Structural Stability and Electronic Structures of InP Nanowires: Role of Surface Dangling Bonds on Nanowire Facets. *Phys. Rev. B: Condens. Matter Mater. Phys.* **2006**, *73* (23), 235308.
(31) Wilhelm, C.; Larrue, A.; Dai, X.; Migas, D.; Soci, C. Anisotropic Photonic Properties of III-V Nanowires in the Zinc-Blende and Wurtzite Phase. *Nanoscale* **2012**, *4* (5), 1446−1454.
(32) Ishizaka, F.; Hiraya, Y.; Tomioka, K.; Fukui, T. Growth of Wurtzite GaP in InP/GaP Core−shell Nanowires by Selective-Area MOVPE. *J. Cryst. Growth* **2015**, *411*, 71−75.
(33) Algra, R. E.; Verheijen, M. A.; Borgström, M. T.; Feiner, L. F.; Immink, G.; Van Enckevort, W. J. P.; Vlieg, E.; Bakkers, E. P. A. M. Twinning Superlattices in Indium Phosphide Nanowires. *Nature* **2008**, *456* (7220), 369−372.
(34) Burgess, T.; Breuer, S.; Caroff, P.; Wong-Leung, J.; Gao, Q.; Hoe Tan, H.; Jagadish, C. Twinning Superlattice Formation in GaAs Nanowires. *ACS Nano* **2013**, *7* (9), 8105−8114.
(35) Glas, F.; Harmand, J. C.; Patriarche, G. Why Does Wurtzite Form in Nanowires of III-V Zinc Blende Semiconductors? *Phys. Rev. Lett.* **2007**, *99* (14), 3−6.
(36) Akiyama, T.; Sano, K.; Nakamura, K.; Ito, T. An Empirical Potential Approach to Wurtzite-Zinc-Blende Polytypism in Group III-V Semiconductor Nanowires. *Japanese J. Appl. Physics, Part 2 Lett.* **2006**, *45* (9), 1275−1278.
(37) Akiyama, T.; Kondo, T.; Tatematsu, H.; Nakamura, K.; Ito, T. Ab Initio Approach to Reconstructions of the InP(111)A Surface: Role of Hydrogen Atoms Passivating Surface Dangling Bonds. *Phys. Rev. B: Condens. Matter Mater. Phys.* **2008**, *78* (20), 1−7.
(38) Li, H.; Sun, Y.; Law, C.; Visbeck, B.; Hicks, F. Reconstructions of the InP(111)A Surface. *Phys. Rev. B: Condens. Matter Mater. Phys.* **2003**, *68* (8), 1−5.

DOI: 10.1021/acs.nanolett.8b03632
Nano Lett. 2018, 18, 7856−7862